

Article

Quantitative Analysis of Photothermal Therapy of Tumor Tissue Using Various Gold Nanoparticle Injection Schemes

Donghyuk Kim  and Hyunjung Kim * 

Department of Mechanical Engineering, Ajou University, Suwon-si 16499, Republic of Korea

* Correspondence: hyunkim@ajou.ac.kr; Tel.: +82-31-219-2340

Abstract: Photothermal therapy is a new chemotherapy technique using photothermal effects, a phenomenon in which light energy is converted into thermal energy. Since the treatment technique is performed without surgical incision, it does not cause bleeding and patients are expected to make rapid recoveries, which are significant advantages. In this study, photothermal therapy with direct injection of gold nanoparticles into tumor tissue was simulated through numerical modeling. The treatment effect resulting from changing the intensity of the irradiated laser, volume fraction of the injected gold nanoparticles, and number of gold nanoparticle injections was quantitatively evaluated. The discrete dipole approximation method was applied to calculate the optical properties of the entire medium, and the Monte Carlo method was applied to identify the absorption and scattering behavior of lasers in tissue. In addition, by confirming the temperature distribution of the entire medium through the calculated light absorption distribution, the treatment effect of photothermal therapy was evaluated, and the optimal treatment conditions were suggested. This is expected to accelerate the popularization of photothermal therapy in the future.

Keywords: apoptosis; direct injection; gold nanoparticles; photothermal therapy; thermal damage



Citation: Kim, D.; Kim, H. Quantitative Analysis of Photothermal Therapy of Tumor Tissue Using Various Gold Nanoparticle Injection Schemes. *Pharmaceutics* **2023**, *15*, 911. <https://doi.org/10.3390/pharmaceutics15030911>

Academic Editors: Heidi Abrahamse and Hanieh Montaseri

Received: 15 February 2023

Revised: 8 March 2023

Accepted: 9 March 2023

Published: 10 March 2023



Copyright: © 2023 by the authors. Licensee MDPI, Basel, Switzerland. This article is an open access article distributed under the terms and conditions of the Creative Commons Attribution (CC BY) license (<https://creativecommons.org/licenses/by/4.0/>).

1. Introduction

Photothermal therapy is a new chemotherapy technique that uses the photothermal effect [1], a phenomenon in which light energy is converted into thermal energy, to increase the temperature of tumor tissues, killing them [2,3]. Since the treatment is performed without incising the affected area, it has the advantages of no bleeding and rapid recovery compared to conventional treatment techniques through incision [4–6]. Light energy, in the form of a laser, is irradiated onto the surface of the skin. Since the energy of the laser cannot be transmitted to great depths, this method has mainly been restricted to research on skin cancer [7,8].

Photothermal therapy primarily utilizes lasers in the near-infrared (NIR) portion of the electromagnetic spectrum. This is because the depth of energy penetration in this range is greater than that of lasers in other wavelength bands. Furthermore, the light absorption coefficient of the medium itself is low in this region, which can reduce unnecessary thermal damage to surrounding tissues [9–11]; however, this also means that NIR irradiation cannot raise the temperature of the medium to the point that induces tumor tissue death. To compensate for this, treatment is performed by administering a light absorption enhancer to tumor tissue to increase the medium's light absorption coefficient at a specific wavelength [12–14]. To achieve this, the light absorption enhancer uses localized surface plasmon resonance (LSPR), a phenomenon that induces collective oscillation of electrons at a specific wavelength [15,16]. Accordingly, it is possible to raise the temperature of the light-absorption enhanced tissue to the range required for biological tissue death, even if a laser in the NIR region is used. Light absorption enhancers are classified according to their constituent materials; among them, gold nanoparticles (GNPs), with excellent biocompatibility, are most common [17–19].

As described above, photothermal therapy aims to kill tumor tissue through temperature increase. To this end, it is first necessary to verify the temperature ranges at which the forms of death of various types of biological tissue occur. In general, the death of biological tissue according to temperature is divided into apoptosis and necrosis [20–22]. Apoptosis is also called cell suicide, and refers to a form of self-destruction which occurs without damaging surrounding tissues. Necrosis, however, involves the destruction of the intracellular contents in the form of leakage and has the possibility of cancer metastasis. Apoptosis is known to be expressed mainly at 43–50 °C, while necrosis is known to occur at higher temperatures. For this reason, it is an important issue in photothermal therapy to maintain the temperature range of apoptosis expression by controlling the appropriate laser conditions.

Photothermal therapy is currently being studied from various perspectives. Muzzi et al. [23] proposed the use of particles with an Fe₃O₄ shell structure on a star-shaped Au core to increase the light conversion efficiency of the light absorption enhancer. Magnetometry and magneto-optical spectroscopy reportedly revealed a pure magnetite shell with excellent saturation magnetization. Furthermore, the plasmonic resonance in the Au@Fe₃O₄ system could be converted to 640 nm, showing applicability for photothermal therapy and visible optical imaging. A preliminary experiment was conducted to irradiate a laser on a cancer cell culture suspension into which Au@Fe₃O₄ was injected, and its suitability for optical response and photothermal therapy was confirmed. Bi et al. [24] proposed Ag₂O₂ nanoparticles, which can control the release of reactive oxygen species, to reduce the toxic side effects of metal peroxide nanoparticles designed to increase oxidative stress. In vitro and in vivo experiments confirmed that Ag₂O₂ nanoparticles had a mortality efficiency of 99.9999% or more within 10 min, provided improved antibacterial and antibiotic membrane functions, and accelerated wound suture against *Staphylococcus aureus* infection with excellent cell and blood compatibility. Through this, a high-efficiency, non-invasive, and safe treatment method for combating bacterial infectious diseases was presented. Wang et al. [25] analyzed the effect of photothermal therapy on tumors containing gold nanoparticles through numerical analysis. The temperature distribution of tumors generated from the skin surface and the surrounding normal tissues was confirmed using the Monte Carlo method, and analysis was performed by varying the treatment conditions for photothermal therapy, such as the tumor size, irradiating laser intensity, and volume fraction of GNPs in the tumor. In addition, the thermal damage to the tissue was confirmed through the Arrhenius thermal damage integral. Yin et al. [26] studied photothermal therapy inside the tissue through numerical analysis. The effects of laser intensity, volume fraction of GNPs, anisotropic scattering characteristics of nanoparticles, and laser incident angle were investigated. Based on this, various treatment strategies, such as single heat source and multiple heat sources, were also identified. In the case of single-dose treatment, it was confirmed that there was almost no difference for the various laser incident angles; in the case of the split treatment, better treatment effects were observed when the laser was irradiated at a constant angle than in the vertical direction. In addition, it was confirmed that multiple heat sources had better therapeutic effects than a single heat source. Guglielmelli et al. [27] developed keratin-coated gold nanoparticles (Ker-AuNPs) as a highly efficient photosensitizing therapeutic agent. The physical, photothermal, chemical, and morphological properties of Ker-AuNPs were investigated by various methods, including dynamic light scattering, ζ-potential, Fourier transform infrared spectroscopy, and X-ray photoelectron spectroscopy. In addition, in vitro experiments were conducted on human glioblastoma cell lines to confirm the efficient cellular absorption, good biocompatibility and local photothermal heating of Ker-AuNPs. Annesi et al. [28] studied an antimicrobial methodology based on gold nanorods (GNRs). The anti-microbial effect of GNRs on *Escherichia coli* bacteria was confirmed, and it is important to control the concentration of GNRs to exclude toxic effects on cells and to generate the amount of heat required to raise the temperature to 50 degrees in about 5 min in the near-infrared region. In addition, as a result of the experiment, it was confirmed that killing efficiency suitable for reducing *Escherichia coli* populations to about 2 log colony-forming units was achieved. Candreva et al. [29] synthesized spherical GNPs

with a diameter of 50 nm coated with polyethylene glycol and administered into *Escherichia coli* cultures to activate plasmon in the visible light region. Experiments were performed in the dark and under laser irradiation, with varying concentrations of GNPs. In the dark, 46% of bacterial growth was inhibited, while laser irradiation at the same concentration resulted in 99% growth inhibition. This was attributed to the fact that the bacterial wall promotes the formation of light-induced clusters of nanoparticles, resulting in an increase in temperature and a bactericidal effect. Furthermore, this photothermal effect is achieved with low intensity laser irradiation only when the pathogen is present, proving that this is an innovative response system to bacterial infections.

Summarizing the preceding studies, research on photothermal therapy under various conditions has been conducted through experiments and numerical analysis. However, although photothermal therapy is a treatment technique based on the heat transfer phenomenon, existing research methods have derived results based on simple phenomenological observations through in vitro and in vivo experiments or quantitative rate of apoptosis, which are commonly used in the biological field. In addition, in the case of thermal damage, only the presence of damage was determined through the Arrhenius thermal damage integral, and it was assumed that GNPs were uniformly distributed in the tumor tissue. There are two main methods of injecting GNPs into tumor tissue: direct injection and intravenous injection [30,31]. Direct injection has the advantage that most of the injected GNPs are located in the tumor tissue; however, the location where they can be injected is limited, and GNPs tend to be concentrated around the injection point. Although intravenous injection allows GNPs to be injected at all locations where blood vessels pass, GNPs are lost in the process of being delivered to the desired location. In the case of direct injection of GNPs into the tumor, the GNPs may have loss from the tumor environment by various immunity mechanisms, but there seems to be less loss of GNPs than in cases of intravenous injection [32].

In this study, numerical analysis was used to study photothermal therapy that simulates the direct injection of GNPs into tumor tissue generated from the skin surface. The target tumor was selected as squamous cell carcinoma, and the four skin layers were implemented through numerical modeling. Analysis was conducted to determine the effect of changing the intensity of the laser and the volume fraction of the injected GNPs, which are some of the variable treatment conditions of photothermal therapy. In addition, for given GNP volume fractions, the effect of varying the number of injections on the effectiveness of photothermal therapy was quantitatively evaluated through the apoptotic variable suggested by Kim et al. [33]. Based on these results, the conditions that produce the optimal photothermal therapy effect were determined for the given treatment situation.

2. Material Properties and Numerical Methods

2.1. Optical Properties of Gold Nanoparticles and Biological Tissues

As mentioned above, photothermal therapy mainly utilizes lasers in the NIR region, and GNPs are injected into the tumor tissue to compensate for the low light absorption coefficient of the tissues in this region. GNPs increase light absorption at a specific wavelength (in this case inside the NIR band) due to the localized surface plasmonic resonance (LSPR) phenomenon.

The optical properties of GNPs were calculated using the discrete dipole approximation (DDA) method [34,35]. The DDA method is a technique capable of calculating the absorption and scattering efficiency of nanoparticles of various shapes. Given a particular shape, the optical efficiency of the particle is obtained by calculating its electromagnetic properties, assuming that the dipoles are located at regular intervals. This technique compensates for the disadvantage that Mie theory can only calculate the shape of a sphere or an ellipse [36].

The first step of the DDA method is calculation of the polarization vector (P), determined through the interaction of the dipole and the local electric field (E) (Equation (2)), as per Equation (1). Here, α and r represent the polarizability and po-

sition vectors, respectively. In Equation (3), $E_{inc,i}$ represents the initial electric field and k represents the wave number. Equation (4) represents the interaction matrix between dipoles. Here, r_{ij} represents $|r_i - r_j|$, and A_{ij} is an interaction matrix under the condition that $i \neq j$. If i and j are equal, the interaction matrix can be simplified to α_i^{-1} .

$$P_i = \alpha_i \cdot E_i(r_i) \quad (1)$$

$$E_i(r_i) = E_{inc,i} - \sum_{j \neq i}^N A_{ij} \cdot P_j (i, j = 1, 2, 3, \dots, N) \quad (2)$$

$$E_{inc,i} = E_0 e^{i(k \cdot r_i)} \quad (3)$$

$$A_{ij} \cdot P_j = \frac{e^{i(k \cdot r_{ij})}}{r_{ij}^3} \left\{ k^2 r_{ij} \times (r_{ij} \times P_j) + \frac{1 - ikr_{ij}}{r_{ij}^2} \times [k^2 P_j - 3r_{ij}(r_{ij} \cdot P_j)] \right\} (i \neq j) \quad (4)$$

The optical cross section C can be calculated as shown in Equations (5)–(7), where $*$ is a complex conjugate symbol.

$$C_{abs} = \frac{4\pi k}{|E_0|^2} \sum_{i=1}^N \left\{ \text{Im} \left[P_i \cdot (\alpha_i^{-1})^* P_i^* \right] - \frac{2}{3} k^3 P_i P_i^* \right\} \quad (5)$$

$$C_{ext} = \frac{4\pi k}{|E_0|^2} \sum_{i=1}^N \text{Im} (E_{inc,i}^* \cdot P_i) \quad (6)$$

$$C_{sca} = C_{ext} - C_{abs} \quad (7)$$

Finally, each optical efficiency Q can be calculated using Equation (8). Here, V and r_{eff} and V are the volume and effective radius of the particle, respectively.

$$Q_{abs} = \frac{C_{abs}}{\pi r_{eff}^2}, Q_{ext} = \frac{C_{ext}}{\pi r_{eff}^2}, Q_{sca} = \frac{C_{sca}}{\pi r_{eff}^2} \quad (8)$$

$$r_{eff} = \left(\frac{3V}{4\pi} \right)^{(1/3)} \quad (9)$$

Each optical efficiency calculated in this way is used in the final optical property calculation. The optical properties of GNPs are obtained from the volume fraction of GNPs (f_v), the effective radius of the particle (r_{eff}), and the optical efficiency Q , calculated through the DDA method as shown in Equation (10) [37]. After the optical properties of the GNPs are calculated, the optical properties of the entire medium with GNPs injected can be calculated as the sum of the optical properties of the GNPs and the optical properties of the medium, as shown in Equation (11) [38].

$$\mu_{abs,np} = 0.75 f_v \frac{Q_{abs,np}}{r_{eff}}, \mu_{sca,np} = 0.75 f_v \frac{Q_{sca,np}}{r_{eff}} \quad (10)$$

$$\mu_{abs} = \mu_{abs,np} + \mu_{abs,m}, \mu_{sca} = \mu_{sca,np} + \mu_{sca,m} \quad (11)$$

2.2. Validation of Numerical Process

In this study, an in vivo experiment using a BALB/c mouse was conducted to verify the proposed numerical analysis modeling. BALB/c mice are an inbred group among laboratory mice and are the most frequently used animals in research fields regarding tumors, inflammation, and autoimmunity. The experiment was conducted in the clean area of Ajou University's Experimental Animal Center and was approved by the Institutional Biosafety Committee (IBC) (No. 2021-0034) and the Institutional Animal Care and Use Committee (IACUC) (No. 2021-0079). Female BALB/c mice with an age of 8 weeks and a weight of 15–20 g, purchased from ORIENT BIO Inc., were used, and experiments were performed while varying the input dose of GNPs. To develop skin cancer in BALB/c mice,

DBMA-TPA two-stage skin carcinogenesis model was applied in this study [39]. The fur of the experimental mouse was shaved 2 days before the onset of carcinogenesis, and 50 μg of 7,12-dimethylbenz(α)anthracene (DMBA) was applied once to the back of the experimental mouse where light was blocked for the onset of carcinogenesis. After 2 weeks of application, 5 μg of 12-O-tetradecanoylphorbol-13-acetate (TPA) was applied to the mouse's back twice a week. Both DMBA and TPA were dissolved in 200 μL of acetone before being applied, and shaving and reagent application were performed with the mouse anesthetized by a respiratory anesthesia machine using isoflurane.

Figure 1 is a schematic of the in vivo experimental for laser irradiation. The laser used in this study is the Cobolt 04-01 Series 'Rumba' model, sold by Cobolt. A 1064 nm single-wavelength laser with an intensity of 0.4 W and a diameter of 1 mm was used, with the beam diameter increased to 10 mm through a beam expander. In addition, an optical mirror was used to change the path of the beam from horizontal to vertical. Since the laser used in this study is in the infrared region, an IR viewer was used to verify the path of the laser beam.

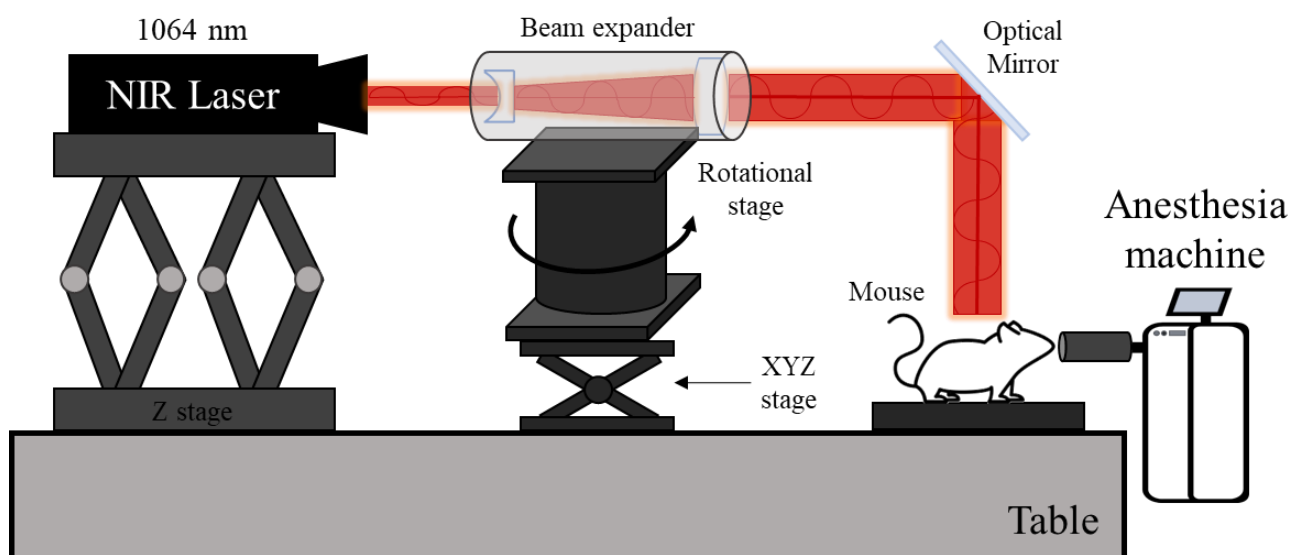


Figure 1. Schematic of in vivo experiment.

Figure 2a,b shows the results on a mouse when laser was irradiated for 5 min on the skin cancer site after injecting 25 μg ($f_v \approx 3 \times 10^{-4}$) and 50 μg ($f_v \approx 6.5 \times 10^{-4}$) of GNPs, respectively. GNPs used in this study are a rod type shape with an effective radius of 10 nm and an aspect ratio of 6.7. They are dispersed at a concentration of 35 $\mu\text{g}/\text{mL}$ in H_2O . GNPs were purchased from Sigma Aldrich and the absorption spectrum of the nanoparticles shows a longitudinal peak at 1064 nm and a longitudinal absorbance OD of 1. As shown in the figure, there were blisters (red circles) on the mice's skin due to burns in the affected area after laser irradiation compared to none before. These were classified as blisters on burns, known to be expressed at about 50–70 $^\circ\text{C}$, as announced by Stoll et al. [40] and Leach et al. [41].

Based on the results of the in vivo experiments, the numerical analysis model proposed in this study was verified. The diameter of the laser was set to 10 mm as in the experiment, and the intensity was set to 0.4 W. The thermal and optical properties of BALB/c mice are summarized in Table 1. Figure 3 shows the results of numerical analysis under the same conditions as in the in vivo experiment. The numerical analysis indicated a maximum temperature of 63.3 $^\circ\text{C}$ when 50 μg ($f_v \approx 6.5 \times 10^{-4}$) of GNPs were injected, with an overall temperature increase to above 50 $^\circ\text{C}$ in the irradiated part. Through this, it can be judged that the results derived from the in vivo experiment and the numerical analysis are similar. In addition, verification of the numerical model was performed through in vitro

experiments using biomimetic phantoms. Comparison between the numerical analysis modeling and the experiment yielded an RMSE of the temperature change over time as an average of 0.1677. It was thus determined that the numerical analysis modeling was valid [33].

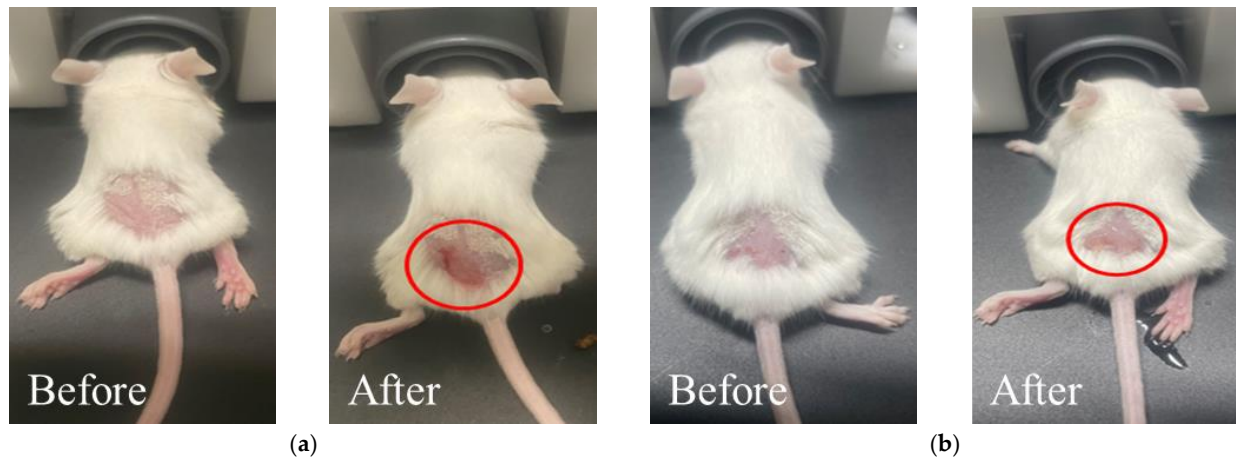


Figure 2. Validation experiment results: (a) 25 µg dose, irradiated for 5 min; (b) 50 µg dose, irradiated for 5 min.

Table 1. Thermal and optical properties of BALB/c mouse [42,43].

Thermal conductivity k_m (W/mK)	0.34
Density ρ (kg/m ³)	1000
Specific heat c_v (J/kgK)	3000
Absorption coefficient μ_{abs} (1/mm)	6.1
Scattering coefficient μ_{sca} (1/mm)	40.65
Anisotropy factor g	0.8

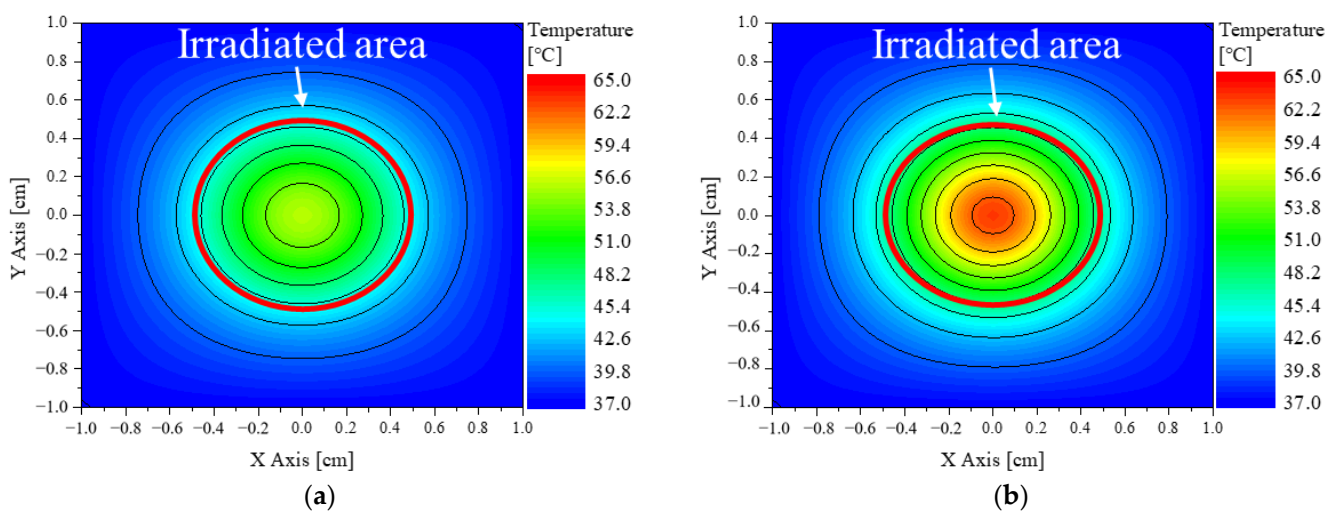


Figure 3. Validation numerical analysis results: (a) 25 µg dose, irradiated for 5 min; (b) 50 µg dose, irradiated for 5 min.

2.3. Numerical Investigation

In this study, the skin implemented in numerical analysis modeling was composed of four layers, including a squamous cell carcinoma generated from the skin surface. As

shown in Figure 4, the squamous cell carcinoma with a radius of 2 mm and a depth of 2 mm was located inside a cylindrical skin layer with a radius of 15 mm and a depth of 20 mm. In order to achieve an appropriate laser penetration depth for the target skin cancer [44], A 1064 nm single-wavelength Gaussian distribution laser with a radius of 2 mm was used as the heat source with the same radius as the tumor. The thickness and thermal and optical properties of each skin layer and tumor tissue are summarized in Table 2.

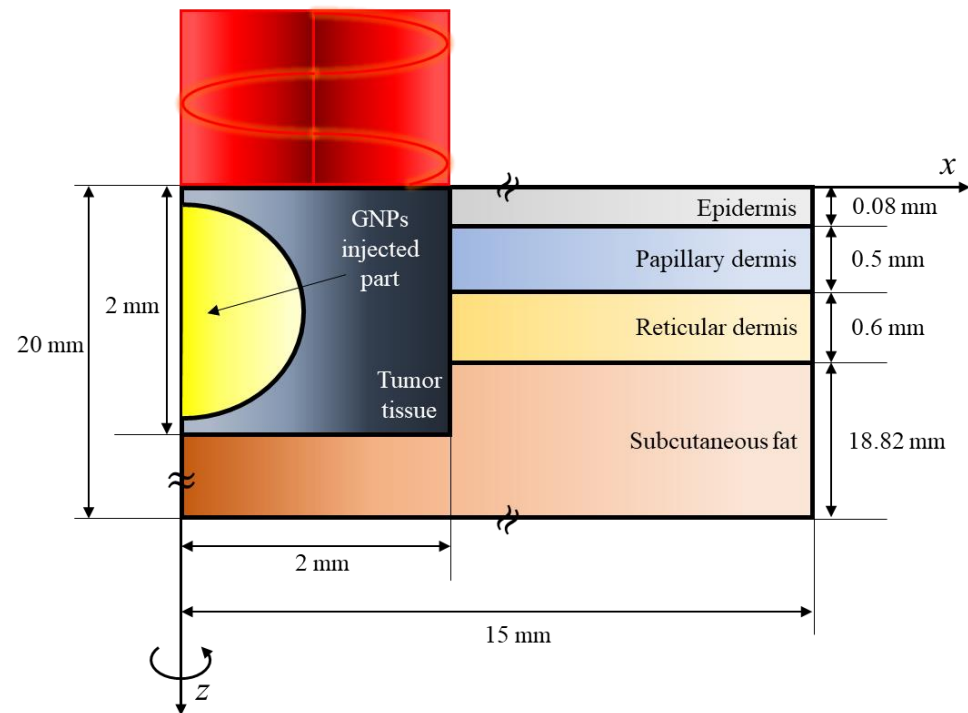


Figure 4. Schematic of numerical model.

Table 2. Properties of skin layer and tumor tissue [11,45–51].

	t (mm)	k_m (W/mK)	ρ (kg/m ³)	c_v (J/kgK)	g	μ_{abs} (1/mm)	μ_{sca} (1/mm)
Epidermis	0.08	0.235	1200	3589	0.8	0.4	45
Papillary dermis	0.5	0.445	1200	3300	0.9	0.38	30
Reticular dermis	0.6	0.445	1200	3300	0.8	0.48	25
Subcutaneous fat	18.82	0.19	1000	2500	0.75	0.43	5
Tumor	2	0.495	1070	3421	0.8	0.047	0.883

In this study, it was assumed that GNPs in the tumor were not uniformly distributed but that GNPs were divided several times and directly injected, resulting in uneven distribution of GNPs inside the tumor. However, in the actual situation, after the GNPs are administered to the tumor tissue, the GNPs are not present only at that site due to various mechanisms. In this study, it was assumed that the treatment was performed immediately after the direct injection of GNPs, and GNPs were present in all the places where they were injected. It was assumed that GNPs were distributed in a spherical shape at each injection site, and the total volume fraction of GNPs in the tumor was assumed to be the same regardless of the number of injections of GNPs. For example, assuming that the initial input volume is 100, it is assumed that when the input is divided 4 times, it is divided into 25 volumetric units in each division. Therefore, the diffusion radius of individual GNPs injection decreases as the number of injections increases, as shown in Figure 5.

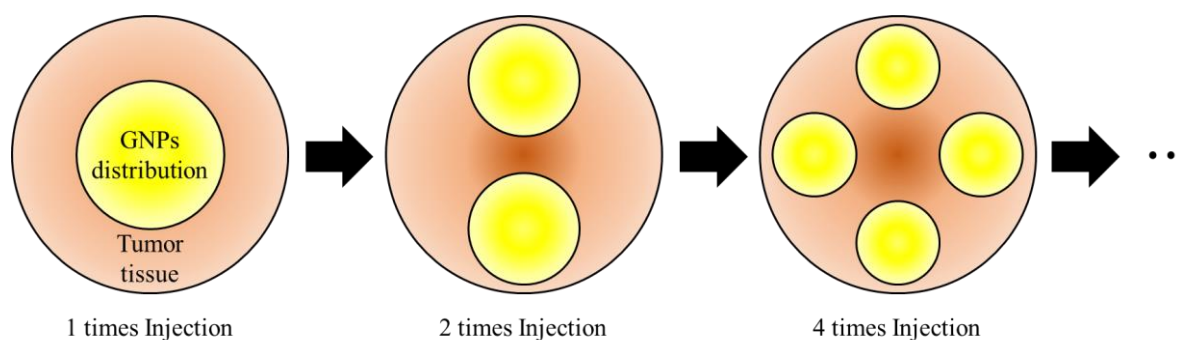


Figure 5. Reduction of the distribution area of GNPs as the number of injection increases.

Table 3 shows the numerical analysis conditions selected in this study. The laser irradiation time was set to 600 s, and the intensity of the laser was increased in 2 mW intervals from 0–100 mW. The volume fraction of injected GNPs was increased from 10^{-1} – 10^{-8} at intervals of 10^{-1} in a total of eight steps. It was assumed that GNPs were distributed in the form of spheres with a diameter of 2 mm for all volume fractions based on one-time injection.

Table 3. Parameters of numerical analysis.

Parameter	Case	Number	Remarks
Laser power (P_l)	0 to 100 mW	51	Intv: 2 mW
Volume fraction of GNPs (f_v)	10^{-1} to 10^{-8}	8	Intv: 10^{-1}
Number of injected GNPs	1 to 6	6	Intv: 1

The GNPs used in the numerical analysis were rod-type nanoparticles with an aspect ratio of 6.67 and an effective radius of 20 nm. The GNPs utilized in the in vivo experiments have an effective radius of 10 nm, but the authors' previous study confirmed that GNPs with an effective radius of 20 nm have the highest absorption efficiency in the rod-type [52]. Therefore, GNPs with an effective radius of 20 nm were utilized in this numerical analysis. It was assumed that the same GNPs were used in all cases, and the wavelength of the irradiating laser was fixed at 1064 nm. Calculated by the DDA method for these particles, the absorption efficiency at 1064 nm is 14.878 and the scattering efficiency is 3.1416. These were applied to Equation (10) to calculate the optical coefficients for different volume fractions. The optical properties of tissues including GNPs were calculated as the sum of the optical properties of the GNPs and those of the medium, calculated through the DDA method, and are summarized in Table 4.

Table 4. Absorption and scattering coefficients of tumor with GNPs.

f_v	10^{-1}	10^{-2}	10^{-3}	10^{-4}	10^{-5}	10^{-6}	10^{-7}	10^{-8}
μ_{abs} (cm^{-1})	5,016,309.16	501,631.34	50,163.55	5016.78	502.10	50.63	5.48	0.97
μ_{sca} (cm^{-1})	1,059,239.60	105,931.91	10,601.14	1068.06	114.75	19.42	9.89	8.94

To calculate the temperature distribution inside the tissue, the absorption distribution of the irradiated laser energy must first be calculated. In this study, a Monte Carlo technique that can consider both absorption and scattering behavior was used to calculate the distribution of light energy absorbed in the medium [53]. The Monte Carlo method is a technique that calculates probabilistically the degree of absorption and scattering of laser particles inside the medium using random numbers. Once the light absorption distribution is calculated, the temperature distribution in the medium can be computed through the explicit finite element method based on the thermal diffusion equation, as shown in

Equation (12). Here, τ , ρ , and c_v represent the time, density, and specific heat, respectively, while F and P_l represent the fluence rate and laser intensity, respectively [54].

$$\Delta T = \frac{\Delta\tau}{\rho c_v} \left(\begin{aligned} &\mu_a F P_l + (T_{x^-} - T) \frac{2k_m k_{m,x^-}}{k_m + k_{m,x^-}} \frac{1}{dx^2} + (T_{x^+} - T) \frac{2k_m k_{m,x^+}}{k_m + k_{m,x^+}} \frac{1}{dx^2} \\ &+ (T_{y^-} - T) \frac{2k_m k_{m,y^-}}{k_m + k_{m,y^-}} \frac{1}{dy^2} + (T_{y^+} - T) \frac{2k_m k_{m,y^+}}{k_m + k_{m,y^+}} \frac{1}{dy^2} \\ &+ (T_{z^-} - T) \frac{2k_m k_{m,z^-}}{k_m + k_{m,z^-}} \frac{1}{dz^2} + (T_{z^+} - T) \frac{2k_m k_{m,z^+}}{k_m + k_{m,z^+}} \frac{1}{dz^2} \end{aligned} \right) \quad (12)$$

Finally, the various conditions for performing photothermal therapy were varied, and the resulting treatment effect for squamous cell cancer was confirmed numerically. Information on how much apoptosis in tumor tissue was maintained, and the thermal damage of surrounding normal tissues was quantitatively confirmed to identify the optimal treatment conditions.

3. Results and Discussion

3.1. Temperature Distribution of Biological Tissues

Figure 6 shows the temperature change over time at the center of the tumor surface with respect to the number of injections and the volume fraction of GNPs (f_v) for lasers of 40 mW intensity. Figure 6a shows the results for an f_v of 10^{-6} , while Figure 6b shows the results when GNPs were deposited in six separate injections, according to volume fractions. As shown in Figure 6a, the temperature of the center of the tumor surface varies according to the number of injections. In particular, when the GNPs were injected separately, excessive temperature rise did not occur, compared to the case in which GNPs were injected once in the center. As shown in Figure 6b, the temperature increase at the center of the tumor surface decreases as the f_v decreases. Through this, it was confirmed that the temperature of the entire medium increased differently according to the various number of injected GNPs and f_v . Accordingly, in the results described later, the temperatures of all points in the medium were checked, and the degree of maintenance of the temperature range where apoptosis occurred and the amount of thermal damage to surrounding normal tissues were quantitatively evaluated.

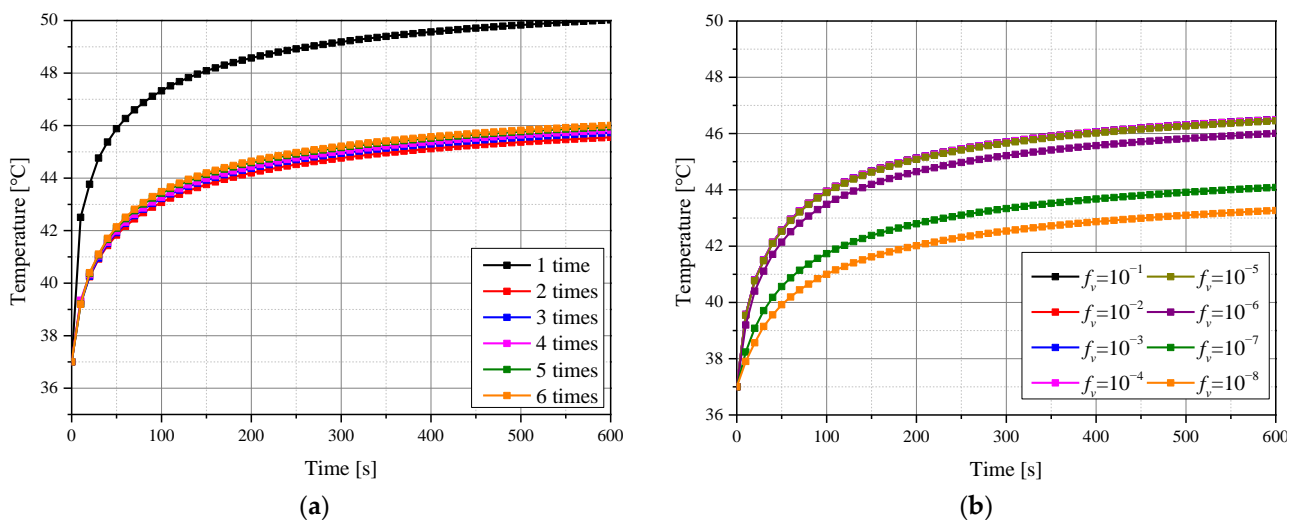


Figure 6. Temperature change of tumor tissue over time for: (a) various numbers of GNPs injections ($f_v = 10^{-6}$); (b) various volume fractions of GNPs (over six injections).

3.2. Apoptosis Occurrence Amount in Tumor Tissue

In this study, the apoptosis retention ratio (θ_A^*) proposed by Kim et al. [29] was used to quantitatively identify how effectively apoptosis occurrence was maintained in the tumor tissue. The term θ_A^* is the average ratio of the tumor volume corresponding to the apoptosis

temperature range of 43–50 °C to the total volume of the tumor at each time step (i.e., to obtain the average, the ratios at each time step are summed and the result is divided by the total treatment time). The maximum value of θ_A^* is 1, indicating that the occurrence temperature range of apoptosis is maintained for the entire treatment time at all locations in the tumor. Using this method, it is possible to quantitatively determine how much the apoptosis occurrence temperature range is maintained inside the tumor tissue during the total treatment time.

Figure 7 shows θ_A^* for each laser intensity P_l according to the various f_v . The tendency of θ_A^* is similar between various numbers of injections, so only the results of the three and six GNP injection cases are replicated in the graphs below. It was confirmed that there existed a P_l corresponding to the maximum θ_A^* for each f_v and for each number of injections. In addition, it was confirmed that as f_v decreased, the P_l corresponding to a maximum θ_A^* increased. This is because a decrease in f_v results in reduced heat absorption capability of the medium for the laser, so a higher P_l is needed to maintain the desired temperature range. As the number of injections increased, the P_l corresponding to a maximum θ_A^* slightly decreased. This is because, as the number of injections increases, the injected GNPs are distributed more widely and evenly, so the tumor tissue is heated in a larger area even at a relatively low P_l .

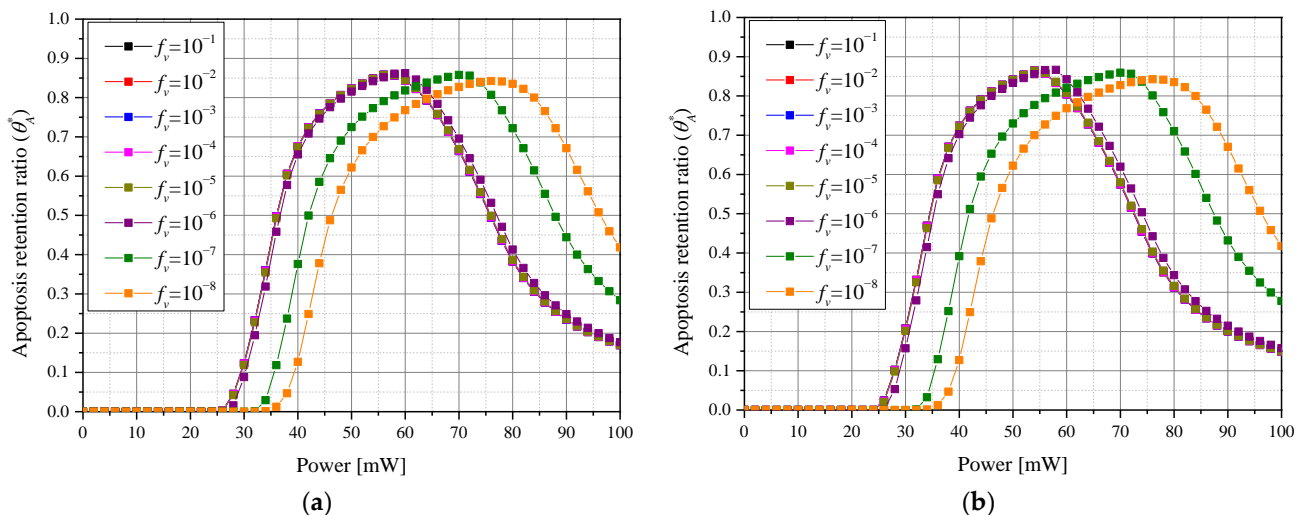


Figure 7. Apoptosis retention ratio (θ_A^*) for various f_v volume fraction of GNPs (f_v) over (a) three injections and (b) six injections.

Figure 8 shows θ_A^* for each P_l according to various number of injected GNPs for a given f_v . Figure 8a shows the change in θ_A^* when f_v is 10^{-3} . In this case, there was a specific P_l corresponding to a maximum θ_A^* for each number of injections. In addition, it was confirmed that the maximum value of θ_A^* was higher when GNPs were injected in two or more divided doses compared to one dose. As mentioned above, this is attributed to the increased GNPs diffusion radius which results in a more widespread temperature rise inside the tumor. Figure 8b shows the result when f_v is 10^{-8} , and it is confirmed that θ_A^* according to P_l is similar for all numbers of injections. This is because the f_v is very low and the effect of the GNPs' injection is insignificant—the GNP injections do initiate an increase in the light absorption coefficient of the entire medium. Evaluating the overall treatment conditions, it was concluded that apoptosis occurrence temperature in tumor tissue was best maintained when the number of injections was five times, f_v was 10^{-5} , and P_l was 58 mW.

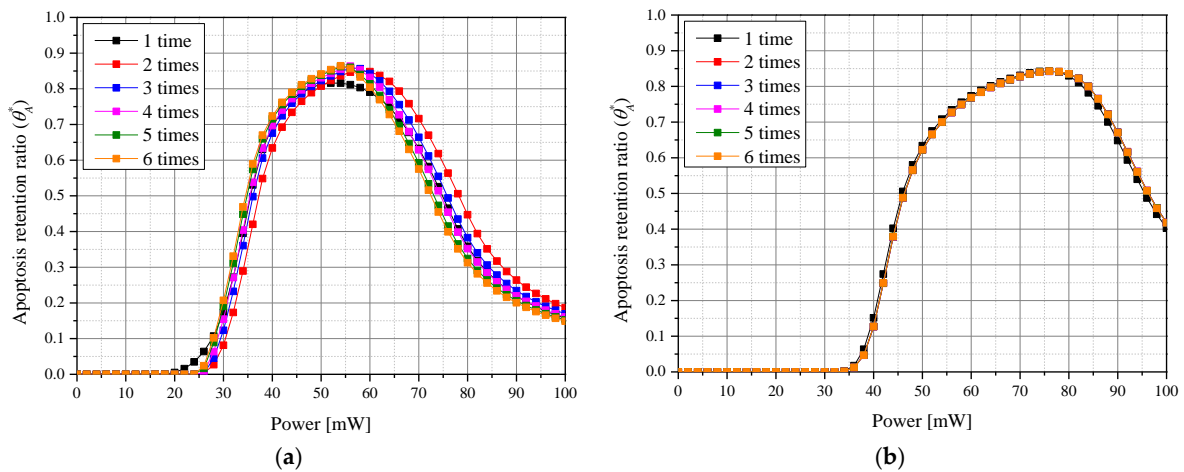


Figure 8. Apoptosis retention ratio (θ_A^*) for various number of GNPs injections at (a) $f_v = 10^{-3}$ and (b) $f_v = 10^{-8}$.

3.3. Thermal Damage of Surrounding Normal Tissues

Previously, the degree to which the apoptosis occurrence temperature was maintained inside the tumor tissue was evaluated through θ_A^* . However, this variable can only identify whether the phenomenon occurs inside the tumor tissue and cannot confirm the amount of thermal damage to the surrounding normal tissue. Accordingly, in this study, the amount of thermal damage to the surrounding normal tissue surrounding the tumor was quantitatively evaluated through the thermal hazard retention value (θ_H^*) [29]. The variable θ_H^* weights the degree to which the phenomena occurred in normal biological tissues according to various temperature ranges, and then averages the weighted sums at each time step for all points in the normal tissues surrounding the tumor tissue. The minimum value of θ_H^* is 1, which indicates that no thermal damage occurs in the surrounding normal tissue, and the value of θ_H^* increases as the thermal damage increases. In this study, only normal tissues from the tumor tissues' end to 50% of the tumor tissue diameter were considered for thermal damage analysis.

Figure 9 shows θ_H^* for each P_l according to f_v . Figure 9a represents the case of three GNPs injections in the tumor tissue, while Figure 6b represents six injections. In both cases, as f_v decreases, the amount of thermal damage to surrounding normal tissues decreases. This is because as f_v decreases, the temperature increase of the tumor tissue occurs less, as shown in Section 3.2.

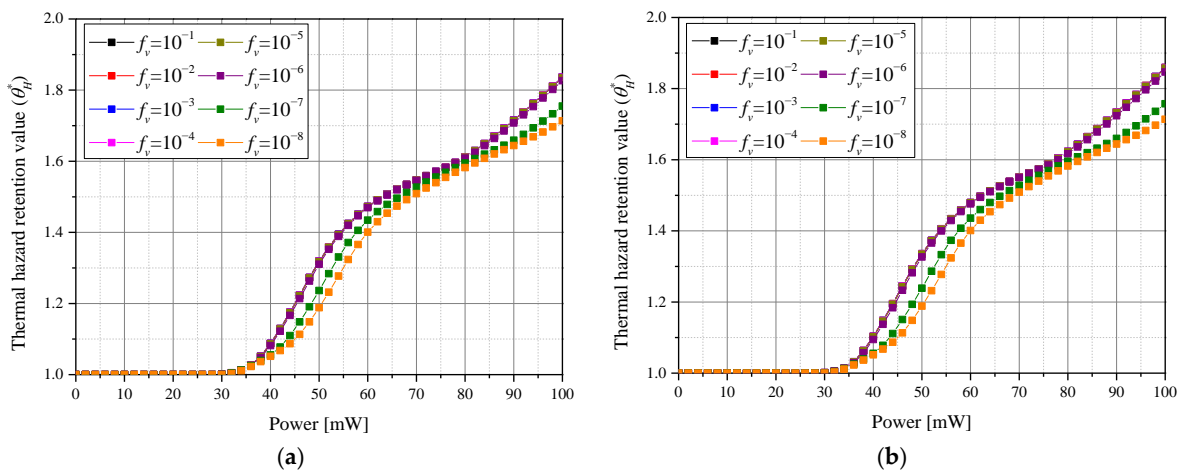


Figure 9. Thermal hazard retention value (θ_H^*) for various volume fractions of GNPs (f_v) over (a) three injections and (b) six injections.

Figure 10a,b shows θ_H^* for each P_l according to the number of GNPs injections when f_v is 10^{-3} and 10^{-8} , respectively. As shown in Figure 10a, as the number of injections increases, so does the amount of thermal damage in the surrounding normal tissue. This is because as the number of injections increases, the diffusion radius of GNPs within the tumor increases, resulting in a temperature rise across a wider range of the tumor tissue, and, as a result, more laser heat absorbed from the tumor tissue is transferred to the surrounding normal tissue.

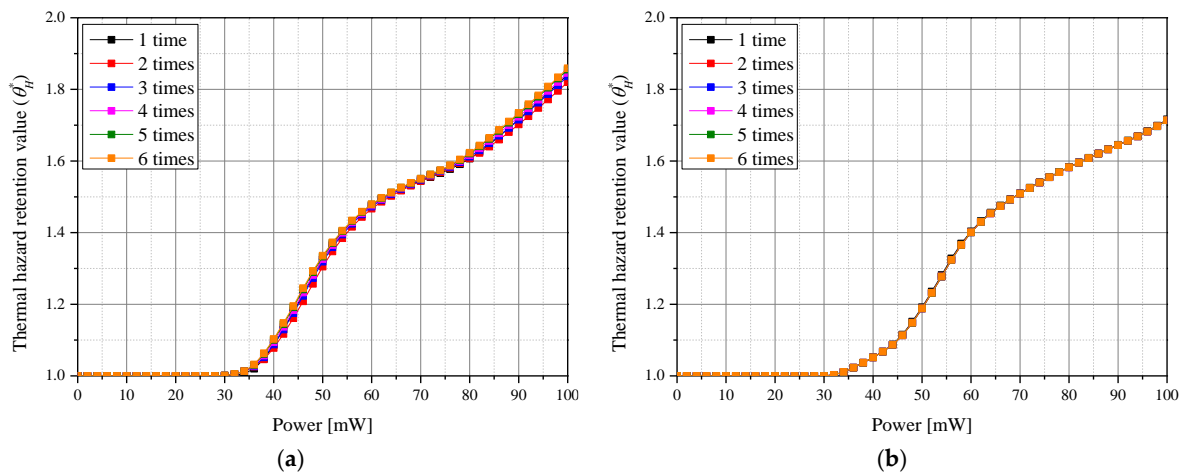


Figure 10. Thermal hazard retention value (θ_H^*) for various numbers of GNPs injections when (a) $f_v = 10^{-3}$ and (b) $f_v = 10^{-8}$.

3.4. Quantitative Analysis of Photothermal Therapy Effect

Sections 3.2 and 3.3 evaluated the degree of maintenance of apoptosis occurrence inside the tumor tissue and the amount of thermal damage to the surrounding normal tissue, respectively. However, since the two phenomena do not occur individually, but rather simultaneously, they should be considered in combination. Therefore, this study identified treatment conditions that maximize the occurrence of apoptosis in tumor tissue and minimize thermal damage to surrounding normal tissues, which is the goal of photothermal therapy. This was accomplished using the effective apoptosis retention ratio (θ_{eff}^*) [29], defined as the ratio of θ_A^* and θ_H^* calculated above. The maximum value of θ_{eff}^* is 1, corresponding to a case where there is no thermal damage at all to the surrounding normal tissue while all points inside the tumor tissue maintained the apoptosis temperature range for all time steps.

Figure 11 shows the resulting θ_{eff}^* at each P_l according to various conditions of photothermal therapy. The trend of the overall graph was derived in the same way as θ_A^* , and it was confirmed that there was a P_l corresponding to an optimal therapeutic effect for each f_v and number of GNPs injections. At P_l values below the optimum point, the temperature of the tumor tissue did not rise sufficiently, resulting in a sub-optimal treatment effect. At values of P_l greater than the optimum point, the temperature of the tumor tissue increased excessively, resulting in significant transfer of laser heat to the surrounding normal tissue, increasing the thermal damage. When summarizing the effects of all treatment conditions, it was confirmed that the optimal treatment effect was achieved when the number of injections was six, f_v was 10^{-3} , and P_l was 42 mW. The optimal P_l for treatment was lower than that for θ_A^* ; this is because a higher P_l results in greater heat transfer from the tumor tissue to the surrounding normal tissue, increasing the amount of thermal damage. Likewise, the higher optimal f_v for treatment vs. θ_A^* is explained as follows: the effect of f_v on heat absorption (caused by the change in the light absorption coefficient) is greater than the effect of laser penetration depth (caused by higher P_l) on the maximum heat absorption depth. Through this analysis, the treatment conditions that produce optimal treatment

effects were identified for the case of photothermal therapy on a skin layer where squamous cell carcinoma has occurred.

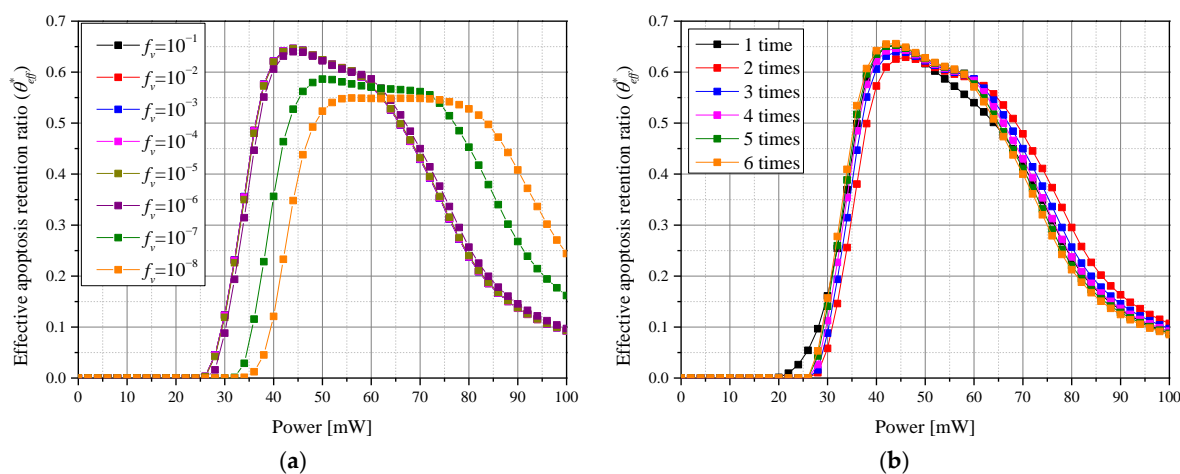


Figure 11. Effective apoptosis retention ratio (θ_{eff}^*) for (a) various f_v values over three GNPs injections; (b) various numbers of GNPs injections for $f_v = 10^{-6}$.

4. Conclusions

In this study, a skin layer in which squamous cell carcinoma occurred was simulated with numerical modeling to evaluate the effect of photothermal therapy under various conditions. To simulate the actual treatment situation, it was assumed that gold nanoparticles were directly injected and partially distributed inside the tumor, and numerical analysis was performed while changing the intensity of the irradiated laser, the volume fraction of the injected gold nanoparticles, and the number of direct injections. To consider the optical effect when gold nanoparticles were administered to tumor tissue, the optical properties of the tissue were calculated by applying the discrete dipole approximation method. In addition, the Monte Carlo method was used to analyze the absorption and scattering behavior of light energy in the medium, and the temperature distribution in the medium was calculated based on the thermal diffusion equation.

Using the obtained temperature distribution, the degree of maintenance of apoptosis occurrence temperature in tumor tissue was derived through the apoptosis retention ratio, and the thermal damage of surrounding normal tissues was calculated through the thermal hazard retention ratio. In addition, to analyze the therapeutic effect of actual treatment conditions, the photothermal therapy conditions that produced optimal therapeutic effects were evaluated through the effective apoptosis retention ratio, which balanced the two ratios above. For the tumor tissue conditions presented in this study, it was concluded that the optimal treatment effect was achieved when the volume fraction of gold particles was 10^{-3} , deposited over six direct injections and irradiated at a laser power of 42 mW. It is thus judged that it is possible to present a reference point for optimal treatment in photothermal therapy in which GNPs are directly injected into the tumor. Furthermore, it is believed that the popularization of photothermal therapy can be accelerated by optimizing treatment conditions from a clinical perspective through the process of performing actual treatment trials. In addition, it is necessary to study a more realistic situation, reflecting the phenomenon that GNPs are dissipated by various mechanisms immediately after they are injected.

Author Contributions: Conceptualization, D.K. and H.K.; Data curation, D.K.; Formal analysis, D.K.; Funding acquisition, H.K.; Investigation, D.K.; Methodology, D.K.; Project administration, H.K.; Resources, H.K.; Software, D.K.; Supervision, H.K.; Validation, D.K.; Visualization, D.K.; Writing—original draft, D.K.; Writing—review and editing, H.K. All authors have read and agreed to the published version of the manuscript.

Funding: This work was supported by a National Research Foundation of Korea (NRF) grant funded by the Korean government (NSIT) (No. NRF-2022R1A2C2012470).

Institutional Review Board Statement: Not applicable.

Informed Consent Statement: Not applicable.

Data Availability Statement: Data sharing is not applicable to this article.

Conflicts of Interest: The authors declare no conflict of interest.

Nomenclature

C	Cross - section area (m^2)
c_v	Specific heat (J/kgK)
E	Electric field (N/C)
f_v	Volume fraction of GNPs
F	Fluence rate ($1/m^2s$)
g	Anisotropy factor
k	wavenumber of radiation ($1/m$)
k_m	Thermal conductivity (W/mK)
P	Polarization vector (C/m^2)
P_l	Intensity of laser (W)
Q	Dimensionless efficiency factor
r	Position vector
r_{eff}	Effective radius of nanoparticle (m)
t	Thickness (m)
T	Temperature (K)

Greek symbols

α	Polarizability (C^2m^2/J)
θ_A^*	Apoptosis retention ratio
θ_{eff}^*	Effective apoptosis retention ratio
θ_H^*	Thermal hazard retention value
μ_{abs}	Absorption coefficient ($1/m$)
μ_{sca}	Scattering coefficient ($1/m$)
ρ	Density (kg/m^3)
τ	Time (s)

Subscripts

abs	Absorption
m	Medium
np	Nanoparticle
sca	Scattering
x, y, z	Notation of direction

Superscripts

$+$	Next element
$-$	Previous element

References

- Almond, D.P.; Patel, P.; Patel, P. *Photothermal Science and Techniques*; Springer Science & Business Media: Berlin/Heidelberg, Germany, 1996.
- Huang, X.; El-Sayed, I.H.; Qian, W.; El-Sayed, M.A. Cancer cell imaging and photothermal therapy in the near-infrared region by using gold nanorods. *J. Am. Chem. Soc.* **2006**, *128*, 2115–2120. [[CrossRef](#)]
- Liu, Y.; Bhattarai, P.; Dai, Z.; Chen, X. Photothermal therapy and photoacoustic imaging via nanotheranostics in fighting cancer. *Chem. Soc. Rev.* **2019**, *48*, 2053–2108. [[CrossRef](#)]
- Abbas, M.; Zou, Q.; Li, S.; Yan, X. Self-assembled peptide-and protein-based nanomaterials for antitumor photodynamic and photothermal therapy. *Adv. Mater.* **2017**, *29*, 1605021. [[CrossRef](#)] [[PubMed](#)]
- Johnson, C.; Serpell, J. Wound infection after abdominal incision with scalpel or diathermy. *Scalpel* **1990**, *130*, 18–95. [[CrossRef](#)]
- Verrier, E.D.; Bossart, K.J.; Heer, F.W. Reduction of infection rates in abdominal incisions by delayed wound closure techniques. *Am. J. Surg.* **1979**, *138*, 22–28. [[CrossRef](#)] [[PubMed](#)]

7. Jung, H.S.; Kong, W.H.; Sung, D.K.; Lee, M.-Y.; Beack, S.E.; Keum, D.H.; Kim, K.S.; Yun, S.H.; Hahn, S.K. Nanographene oxide–hyaluronic acid conjugate for photothermal ablation therapy of skin cancer. *ACS Nano* **2014**, *8*, 260–268. [[CrossRef](#)]
8. Abo-Elfadl, M.T.; Gamal-Eldeen, A.M.; Elshafey, M.M.; Abdalla, G.M.; Ali, S.S.; Ali, M.R.; Zawrah, M.F. Photothermal therapeutic effect of PEGylated gold nano-semicubes in chemically-induced skin cancer in mice. *J. Photochem. Photobiol. B Biol.* **2016**, *164*, 21–29. [[CrossRef](#)] [[PubMed](#)]
9. Mustafa, F.; Jaafar, M. Comparison of wavelength-dependent penetration depths of lasers in different types of skin in photodynamic therapy. *Indian J. Phys.* **2013**, *87*, 203–209. [[CrossRef](#)]
10. Ash, C.; Dubec, M.; Donne, K.; Bashford, T. Effect of wavelength and beam width on penetration in light-tissue interaction using computational methods. *Lasers Med. Sci.* **2017**, *32*, 1909–1918. [[CrossRef](#)]
11. Salomatina, E.V.; Jiang, B.; Novak, J.; Yaroslavsky, A.N. Optical properties of normal and cancerous human skin in the visible and near-infrared spectral range. *J. Biomed. Opt.* **2006**, *11*, 064026. [[CrossRef](#)]
12. Chen, Y.; Gao, Y.; Chen, Y.; Liu, L.; Mo, A.; Peng, Q. Nanomaterials-based photothermal therapy and its potentials in antibacterial treatment. *J. Control. Release* **2020**, *328*, 251–262. [[CrossRef](#)] [[PubMed](#)]
13. Jung, H.S.; Verwilt, P.; Sharma, A.; Shin, J.; Sessler, J.L.; Kim, J.S. Organic molecule-based photothermal agents: An expanding photothermal therapy universe. *Chem. Soc. Rev.* **2018**, *47*, 2280–2297. [[CrossRef](#)]
14. Song, X.; Chen, Q.; Liu, Z. Recent advances in the development of organic photothermal nano-agents. *Nano Res.* **2015**, *8*, 340–354. [[CrossRef](#)]
15. Hutter, E.; Fendler, J.H. Exploitation of localized surface plasmon resonance. *Adv. Mater.* **2004**, *16*, 1685–1706. [[CrossRef](#)]
16. Willets, K.A.; Van Duyne, R.P. Localized surface plasmon resonance spectroscopy and sensing. *Annu. Rev. Phys. Chem.* **2007**, *58*, 267–297. [[CrossRef](#)]
17. El-Sayed, I.H.; Huang, X.; El-Sayed, M.A. Selective laser photo-thermal therapy of epithelial carcinoma using anti-EGFR antibody conjugated gold nanoparticles. *Cancer Lett.* **2006**, *239*, 129–135. [[CrossRef](#)]
18. Huang, X.; El-Sayed, M.A. Gold nanoparticles: Optical properties and implementations in cancer diagnosis and photothermal therapy. *J. Adv. Res.* **2010**, *1*, 13–28. [[CrossRef](#)]
19. Huang, X.; Jain, P.K.; El-Sayed, I.H.; El-Sayed, M.A. Determination of the minimum temperature required for selective photothermal destruction of cancer cells with the use of immunotargeted gold nanoparticles. *Photochem. Photobiol.* **2006**, *82*, 412–417. [[CrossRef](#)] [[PubMed](#)]
20. Hawes, M.C.; Wheeler, H. Factors affecting victorin-induced root cap cell death: Temperature and plasmolysist. *Physiol. Plant Pathol.* **1982**, *20*, 137–144. [[CrossRef](#)]
21. Kerr, J.F.; Wyllie, A.H.; Currie, A.R. Apoptosis: A basic biological phenomenon with wideranging implications in tissue kinetics. *Br. J. Cancer* **1972**, *26*, 239–257. [[CrossRef](#)]
22. Wyllie, A.H. Cell death. *Cytol. Cell Physiol.* **1987**, *361*, 755–785.
23. Muzzi, B.; Albino, M.; Gabbani, A.; Omelyanchik, A.; Kozenkova, E.; Petrecca, M.; Innocenti, C.; Balica, E.; Lavacchi, A.; Scavone, F. Star-Shaped Magnetic-Plasmonic Au@Fe₃O₄ Nano-Heterostructures for Photothermal Therapy. *ACS Appl. Mater. Interfaces* **2022**, *14*, 29087–29098. [[CrossRef](#)]
24. Bi, X.; Bai, Q.; Liang, M.; Yang, D.; Li, S.; Wang, L.; Liu, J.; Yu, W.W.; Sui, N.; Zhu, Z. Silver peroxide nanoparticles for combined antibacterial sonodynamic and photothermal therapy. *Small* **2022**, *18*, 2104160. [[CrossRef](#)] [[PubMed](#)]
25. Wang, S.-L.; Qi, H.; Ren, Y.-T.; Chen, Q.; Ruan, L.-M. Optimal temperature control of tissue embedded with gold nanoparticles for enhanced thermal therapy based on two-energy equation model. *J. Therm. Biol.* **2018**, *74*, 264–274. [[CrossRef](#)] [[PubMed](#)]
26. Yin, Y.; Ren, Y.; Li, H.; Qi, H. Characteristic analysis of light and heat transfer in photothermal therapy using multiple-light-source heating strategy. *Int. J. Therm. Sci.* **2020**, *158*, 106533. [[CrossRef](#)]
27. Guglielmelli, A.; Rosa, P.; Contardi, M.; Prato, M.; Mangino, G.; Miglietta, S.; Petrozza, V.; Pani, R.; Calogero, A.; Athanassiou, A.; et al. Biomimetic keratin gold nanoparticle-mediated in vitro photothermal therapy on glioblastoma multiforme. *Nanomedicine* **2020**, *16*, 121–138. [[CrossRef](#)]
28. Annesi, F.; Pane, A.; Losso, M.A.; Guglielmelli, A.; Lucente, F.; Petronella, F.; Placido, T.; Comparelli, R.; Guzzo, M.G.; Curri, M.L.; et al. Thermo-plasmonic killing of Escherichia coli TG1 bacteria. *Materials* **2019**, *12*, 1530. [[CrossRef](#)]
29. Candreva, A.; De Rose, R.; Perrotta, I.D.; Guglielmelli, A.; La Deda, M. Light-Induced Clusterization of Gold Nanoparticles: A New Photo-Triggered Antibacterial against *E. coli* Proliferation. *Nanomaterials* **2023**, *13*, 746. [[CrossRef](#)] [[PubMed](#)]
30. Terentyuk, G.S.; Maslyakova, G.N.; Suleymanova, L.V.; Khlebtsov, B.N.; Kogan, B.Y.; Akchurin, G.G.; Shantrocha, A.V.; Maksimova, I.L.; Khlebtsov, N.G.; Tuchin, V.V. Circulation and distribution of gold nanoparticles and induced alterations of tissue morphology at intravenous particle delivery. *J. Biophotonics* **2009**, *2*, 292–302. [[CrossRef](#)]
31. Ko, W.-K.; Lee, S.J.; Kim, S.J.; Han, G.H.; Han, I.-b.; Hong, J.B.; Sheen, S.H.; Sohn, S. Direct injection of hydrogels embedding gold nanoparticles for local therapy after spinal cord injury. *Biomacromolecules* **2021**, *22*, 2887–2901. [[CrossRef](#)] [[PubMed](#)]
32. Dimitriou, N.M.; Tsekenis, G.; Balanikas, E.C.; Pavlopoulou, A.; Mitsiogianni, M.; Mantso, T.; Pashos, G.; Boudouvis, A.G.; Lykakis, L.N.; Tsigaridas, G.; et al. Gold nanoparticles, radiations and the immune system: Current insights into the physical mechanisms and the biological interactions of this new alliance towards cancer therapy. *Pharmacol. Ther.* **2017**, *178*, 1–17. [[CrossRef](#)] [[PubMed](#)]
33. Kim, D.; Kim, H. Induction of apoptotic temperature in photothermal therapy under various heating conditions in multi-layered skin structure. *Int. J. Mol. Sci.* **2021**, *22*, 11091. [[CrossRef](#)] [[PubMed](#)]

34. Draine, B.T.; Flatau, P.J. Discrete-dipole approximation for scattering calculations. *Josa A* **1994**, *11*, 1491–1499. [[CrossRef](#)]
35. Draine, B.T.; Flatau, P.J. Discrete-dipole approximation for periodic targets: Theory and tests. *Josa A* **2008**, *25*, 2693–2703. [[CrossRef](#)]
36. Mie, G. Contributions to the optics of turbid media, particularly of colloidal metal solutions. *Contrib. Opt. Turbid. Media* **1976**, *25*, 377–445.
37. Dombrovsky, L.A.; Timchenko, V.; Jackson, M.; Yeoh, G.H. A combined transient thermal model for laser hyperthermia of tumors with embedded gold nanoshells. *Int. J. Heat Mass Transf.* **2011**, *54*, 5459–5469. [[CrossRef](#)]
38. Vera, J.; Bayazitoglu, Y. Gold nanoshell density variation with laser power for induced hyperthermia. *Int. J. Heat Mass Transf.* **2009**, *52*, 564–573. [[CrossRef](#)]
39. Vähätupa, M.; Pemmari, T.; Juntila, I.; Pesu, M.; Järvinen, T.A. Chemical-induced skin carcinogenesis model using dimethylbenz[a]anthracene and 12-o-tetradecanoyl phorbol-13-acetate (DMBA-TPA). *J. Vis. Exp.* **2019**, *154*, e60445. [[CrossRef](#)] [[PubMed](#)]
40. Stoll, A.M.; Chianta, M.A. Heat transfer through fabrics as related to thermal injury. *Trans. N. Y. Acad. Sci.* **1971**, *33*, 649–670. [[CrossRef](#)]
41. Leach, E.; Peters, R.; Rossiter, R. Experimental thermal burns, especially the moderate temperature burn. *Q. J. Exp. Physiol. Cogn. Med. Sci. Transl. Integr.* **1943**, *32*, 67–86. [[CrossRef](#)]
42. Mi, Y.; Yao, C.; Li, C.; Sun, C.; Tang, J.; Yang, F.; Wen, Y. Caspase-3 activation by exponential decay nanosecond pulsed electric fields on tumor-bearing BALB/c nude mice in vivo. *IEEE Trans. Plasma Sci.* **2010**, *38*, 1963–1971.
43. Krainov, A.; Mokeeva, A.; Sergeeva, E.; Agrba, P.; Kirillin, M.Y. Optical properties of mouse biotissues and their optical phantoms. *Opt. Spectrosc.* **2013**, *115*, 193–200. [[CrossRef](#)]
44. Ganathan, P.; Rao, A.P.; Singaravelu, G.; Manickam, E. Review of laser in nanophotonics—a literature study for cellular mechanism. *J. Cancer Biol. Res.* **2017**, *5*, 1094.
45. Çetingül, M.P.; Herman, C. A heat transfer model of skin tissue for the detection of lesions: Sensitivity analysis. *Phys. Med. Biol.* **2010**, *55*, 5933. [[CrossRef](#)] [[PubMed](#)]
46. Çetingül, M.P.; Herman, C. Quantification of the thermal signature of a melanoma lesion. *Int. J. Therm. Sci.* **2011**, *50*, 421–431. [[CrossRef](#)]
47. Holmer, C.; Lehmann, K.-S.; Wanken, J.; Reissfelder, C.; Roggan, A.; Müller, G.J.; Buhr, H.-J.; Ritz, J.-P. Optical properties of adenocarcinoma and squamous cell carcinoma of the gastroesophageal junction. *J. Biomed. Opt.* **2007**, *12*, 014025. [[CrossRef](#)]
48. Jiang, S.; Ma, N.; Li, H.; Zhang, X. Effects of thermal properties and geometrical dimensions on skin burn injuries. *Burns* **2002**, *28*, 713–717. [[CrossRef](#)] [[PubMed](#)]
49. Prasad, B.; Kim, S.; Cho, W.; Kim, S.; Kim, J.K. Effect of tumor properties on energy absorption, temperature mapping, and thermal dose in 13.56-MHz radiofrequency hyperthermia. *J. Therm. Biol.* **2018**, *74*, 281–289. [[CrossRef](#)]
50. Torvi, D.; Dale, J. A finite element model of skin subjected to a flash fire. *J. Biomech. Eng.* **1994**, *116*, 250–255. [[CrossRef](#)]
51. Wilson, S.B.; Spence, V.A. A tissue heat transfer model for relating dynamic skin temperature changes to physiological parameters. *Phys. Med. Biol.* **1988**, *33*, 895. [[CrossRef](#)]
52. Kim, D.; Kim, H. Numerical Study on Death of Squamous Cell Carcinoma Based on Various Shapes of Gold Nanoparticles Using Photothermal Therapy. *Sensors* **2022**, *22*, 1671. [[CrossRef](#)] [[PubMed](#)]
53. Wang, L.; Jacques, S.L.; Zheng, L. MCML—Monte Carlo modeling of light transport in multi-layered tissues. *Comput. Methods Programs Biomed.* **1995**, *47*, 131–146. [[CrossRef](#)] [[PubMed](#)]
54. Marti, D.; Aasbjerg, R.N.; Andersen, P.E.; Hansen, A.K. MCmatlab: An open-source, user-friendly, MATLAB-integrated three-dimensional Monte Carlo light transport solver with heat diffusion and tissue damage. *J. Biomed. Opt.* **2018**, *23*, 121622. [[CrossRef](#)] [[PubMed](#)]

Disclaimer/Publisher’s Note: The statements, opinions and data contained in all publications are solely those of the individual author(s) and contributor(s) and not of MDPI and/or the editor(s). MDPI and/or the editor(s) disclaim responsibility for any injury to people or property resulting from any ideas, methods, instructions or products referred to in the content.